Journal of Materials Chemistry

Cite this: *J. Mater. Chem.*, 2012, **22**, 4963

www.rsc.org/materials

PAPER

Dual-heteroatom-modified ordered mesoporous carbon: Hydrothermal functionalization, structure, and its electrochemical performance†

Xiaochen Zhao,[abe] Qiang Zhang,[ac] Bingsen Zhang,[a] Cheng-Meng Chen,[ae] Aiqin Wang,[b] Tao Zhang*[b] and Dang Sheng Su*[ad]

Received 12th November 2011, Accepted 22nd December 2011
DOI: 10.1039/c2jm15820e

The diverse applications of ordered mesoporous carbons (OMCs) are not only bonded to their superior structural properties, but also to their chemical properties. The termination of graphene sheets in OMCs provides abundant sites for heteroatom decoration to mediate their chemical properties. In this contribution, boron and phosphorus were co-incorporated into OMCs *via* a facile aqueous self-assembly taking advantage of a hydrothermal doping strategy. The as-obtained B/P-modified OMCs process a large surface area of *ca.* 600 $m^2 g^{-1}$, and a uniform pore size of *ca.* 6.3 nm, as well as long range ordering. By varying the hydrothermal synthesis temperature, the concentration of B and P introduced can be controlled from 0.8 to 1.6 wt% and from 2.3 to 3.6 wt%, respectively. The interaction of heteroatom B and P was enhanced when the hydrothermal temperature is above 100 °C. The heteroatom-containing groups were firmly embedded and homogeneously distributed on the carbon frameworks. When the B/P co-modified OMCs were applied as electrodes in supercapacitors, they presented promising performance compared with B- or/and P-modified OMC obtained without hydrothermal treatment.

1. Introduction

Porous carbon materials afford large pore volume, hierarchical pore structure, high specific surface area, and large adsorption capacities for gaseous, liquid, or ion adsorption.[1] They are used as electrode materials for supercapacitors, batteries and fuel cells, as supports for catalytic reactions and as sorbents for chromatography, gas separation and water purification.[1] Besides the common feature of high surface area bearing from various porous carbon materials, ordered mesoporous carbons (OMCs) are further improved with periodically arranged uniform mesopore space, alternative pore shapes, and tunable pore sizes.[1] Thus, they are very attractive for advanced applications in energy conversion and heterogeneous catalysis. However, the diverse applications of OMCs are not only bonded to their superior physical properties, such as mesostructural associated parameters, electric and thermal conductivity, but also to their chemical reactivities.

In OMC materials, some carbon atoms in the sp^2 hybridized state afford semi-metal properties with a small number of metallic electrons that can be available on the surface.[2] Generally, the termination of carbon sheets in OMCs requires foreign atoms to saturate dangling bonds.[3] Thus, the intrinsic chemical properties of OMCs can be easily modified by the heteroatom functionalization on graphene geometries such as at the edges, defects or strained regions.[4] Great effort has been paid to develop heteroatom (such as B, N, O, P, S) incorporated OMCs as advanced electrode materials in electrochemical energy storage and as an alternative to current catalysts for biomass conversion. For instance, both the nitrogen-doped ordered mesoporous graphitic arrays[5] and metal-free nitrogen-containing nanocarbon[6] can cause electron modulation to provide desirable electronic structures with relatively good electro-catalytic activity and long-term stability toward the oxygen reduction reaction for fuel cells; the B-,[7–10] O-,[11–13] N-,[9,11,12,14] and P-incorporated[8,12,15] OMCs exhibited superior electrochemical performances to their non-incorporated counterparts when used as supercapacitor electrodes; heteroatoms (such as B, N, P, S) increase the activity and/or selectivity in triglyceride transesterification,[16] oxidative dehydrogenation and alkane activation

[a]*Department of Inorganic Chemistry, Fritz Haber Institute of the Max Planck Society, Faradayweg 4–6, Berlin, 14195, Germany. E-mail: dangsheng@fhi-berlin.mpg.de*
[b]*State Key Laboratory of Catalysis, Dalian Institute of Chemical Physics, Chinese Academy of Science, PO Box 110, Dalian, 116023, P. R. China. E-mail: taozhang@dicp.ac.cn; Fax: +86-411-84691570; Tel: +86-411-84379015*
[c]*Beijing Key Laboratory of Green Chemical Reaction Engineering and Technology, Department of Chemical Engineering, Tsinghua University, Beijing, 100084, P. R. China*
[d]*Catalysis and Materials Division, Shenyang National Laboratory for Materials Science, Institute of Metal Research, Chinese Academy of Sciences, 72 Wenhua Road, Shenyang, 110016, P. R. China*
[e]*Graduate University of Chinese Academy of Science, Beijing, 100049, P. R. China*
† Electronic supplementary information (ESI) available. See DOI: 10.1039/c2jm15820e

reactions[17] on nanocarbon and OMCs; N-doped OMC with a graphitic wall structure was a good metal-free basic catalyst[18] and catalyst support.[19] Recently, the phosphorus-doped porous carbon nitride was reported to present not only a much better electrical conductivity but also an improvement in photocurrent generation,[20] which is interesting for polymeric batteries.

Incorporation of one kind of heteroatom into OMCs or nanocarbon frameworks has been widely investigated and presented excellent performances in sustainable chemistry. Nevertheless, whether two kinds of heteroatoms incorporation will strengthen or weaken the modifying effect, or even exhibit a bi-functional or synergistic effect, as bi-metallic catalysts or alloys do, is still an open question. To fully demonstrate the potential applications of dual-modified OMCs, as well as allow mechanistic insight into the roles that heteroatoms play, the manipulation of dual-heteroatom-containing functional groups on OMCs becomes scientifically necessary.

In this contribution, we explored the idea of synthesis of B/P dual-heteroatom-incorporated OMCs by a facile hydrothermal self-assembly together with a carbonization strategy and explored their chemical structure and electrochemical performance for supercapacitors. The supercapacitors are gaining increasing attention for complementing batteries in hybrid electric vehicles, portable electronics, and industrial power managements because of their large power density, moderate energy density, and long cycle-life.[21] Briefly, boric acid, phosphoric acid, and resorcinol were employed as B, P, and C sources, and tri-copolymer F127 as the structure-directing agent for polymerization. The mixture of resorcinol, boric acid, and phosphoric acid polymerize with formaldehyde, and free hydroxyl groups in the benzene rings could co-assemble with F127 *via* hydrogen bonds and form a mesostructure by a hydrothermal process, which is an efficient and green way for materials synthesis.[22] The resultant B/P-containing precursor was then carbonized under Ar atmosphere at 600 °C to obtain OMCs with different B/P contents. Their textural structure, chemical bonding, and thermal stability was investigated by N_2 adsorption, X-ray diffraction (XRD), transmission electron microscopy (TEM), electron energy loss spectroscopy (EELS), inductively coupled plasma spectrometer (ICP), X-ray photoelectron spectroscopy (XPS), and thermal gravimetry-mass spectrometry (TG-MS). The electrochemical properties of the B/P dual-incorporated OMCs were evaluated as electrodes of supercapacitors.

2. Results and discussion

2.1 Textural structure of B/P co-modified OMCs

Fig. 1a depicts the nitrogen adsorption isotherms and BJH pore size distribution of HTBP50, HTBP100, and HTBP150. The typical type IV isotherms with well-defined H1 hysteresis loops were characteristic of mesostructure and the narrow BJH distribution showed the well defined, uniform pore size of the HTBPs. According to BJH adsorption curves, the average mesopore sizes of HTBPs were all centred at *ca.* 6.3 nm (Fig. 1b), suggesting that different hydrothermal (HT) temperatures have little influence on the formation and size of the F127 micelle, as well as organic–organic self-assembly which finally determined

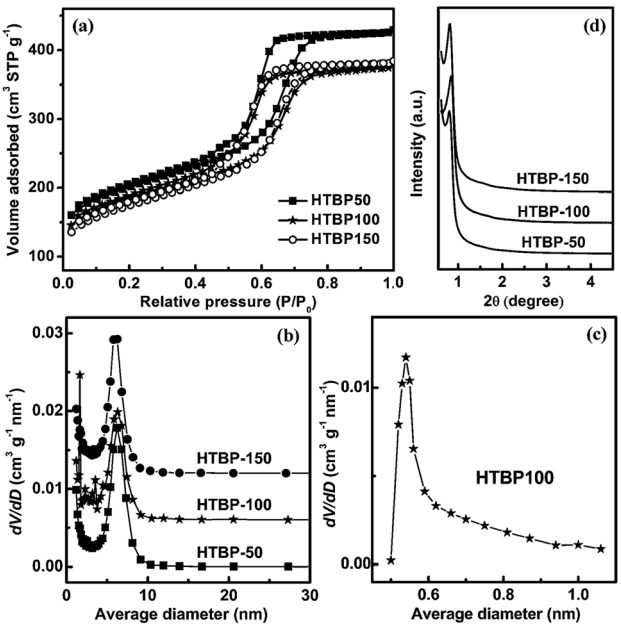

Fig. 1 (a) N_2 sorption isotherms, (b) mesopore size distributions and (d) low-angle XRD patterns of HTBP50, HTBP100 and HTBP150; (c) micropore size distribution of HTBP100.

the pore size. However, when the HT temperature increased from 50 to 100 °C, a drop in pore volume was observed from 0.67 to 0.59 $cm^3\ g^{-1}$. This indicates that the polymerization of resorcinol and formaldehyde benefits from the higher HT temperature and consequently results in a condenser precursor even in presence of B and P. However, the pore volume of HTBP150 showed no obvious difference with HTBP100 suggesting that the temperature of 100 °C is high enough for thorough precursor polymerization. Moreover, a large increase of adsorption volume at a low P/P_0 (less than 0.5) indicates the presence of micropores. To further reveal the structural details, micropore analysis was conducted on HTBP100 and the micropore size calculated according to the Horvath–Kawazoe equation was 0.6 nm (Fig. 1c). Fig. 1d presented the low-angle XRD patterns, one peak centred at $2\theta = 0.5{\sim}1^\circ$ was observed for all HTBPs, indicating that the obtained B/P-modified carbons afford a highly ordered mesostructure over a long range. As well as XRD patterns, the TEM images of HTBP50, HTBP100, and HTBP150 (Fig. 2) showed long channels along the (100) direction and cross-section along the (001) direction, indicating a well preserved typical 2D hexagonal structure. The cell size of the mesopores, measured according to TEM images (11.3 nm of HTBP100, for example) is consistent with its cell parameter (11.7 nm) that is calculated by the low-angle XRD pattern. Table 1 summarized the textural parameters of these B/P-modified mesoporous carbon materials.

2.2 Chemical structure of B/P co-modified OMCs

The introduction of B and P elements into the carbon frameworks can be confirmed by ICP (Table 1), energy filtered TEM (EFTEM) images (Fig. 3a), EELS (Fig. 3b) and XPS (Fig. 4). Using elemental mapping under EFTEM mode, the distribution of heteroatom modification can be directly obtained from

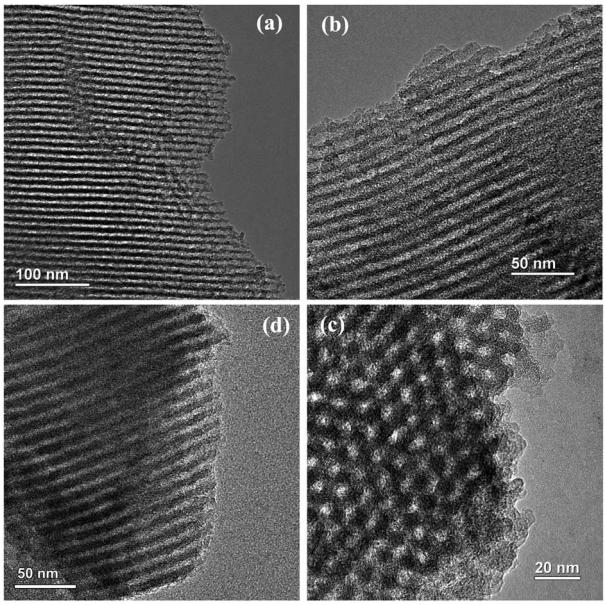

Fig. 2 TEM micrographs of (a) HTBP50, (b,c) HTBP100, and (d) HTBP150.

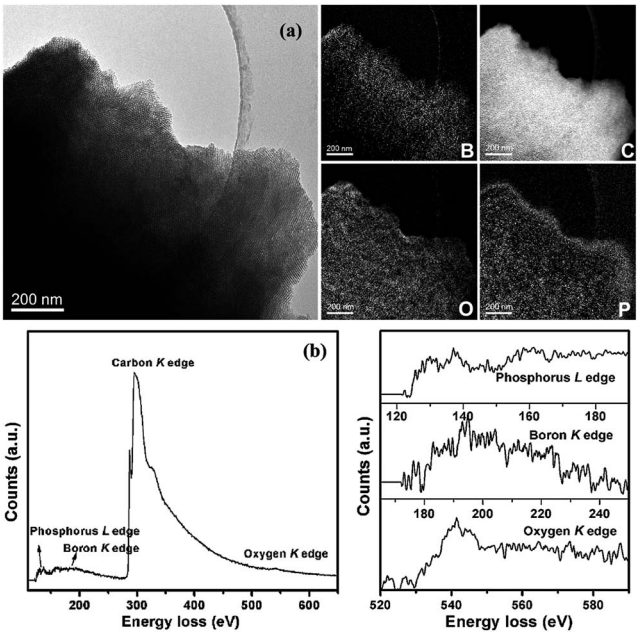

Fig. 3 (a) EFTEM of HTBP100: zero loss image, B, C, O and P energy-filtered images and (b) EELS spectrum of HTBP100.

EFTEM images, as shown in Fig. 3a. It indicates that B, O, and P were homogeneously distributed on the carbon framework, and more P functional groups were distributed on the edge due to the self-adsorption of released P species. The EELS spectra taken from the modified mesoporous carbon showed the simultaneous presence of C, B, P, and O elements (Fig. 3b shows spectra of C, B, P, and O).

XPS analysis was conducted to further confirm the EELS results and designated B and P functional groups along with different HT temperatures. As shown in Fig. 4 and Fig. S1,† the content of B remarkably increases from 0.8 to 1.6 wt%, the content of P increases from 2.3 to 3.6 wt% and that of O increases from 8.1 to 10.0 wt% when increasing the HT temperature from 50 to 150 °C. This is in good agreement with ICP results with a tolerant deviation. The B and P species were further determined by XPS fine scanning. As shown in Fig. 4, the O_{1s} spectral curves were fitted into five established groups with fixed energy positions centred at 531.1, 532.3, 533.3, 534.2, and 535.9 eV, and assigned to the species of quinone, C=O, C–O, C–OH, and adsorbed H_2O respectively.[24] Whereas the P_{2p} spectrum is comprised of $2P_{3/2}$ and $2P_{1/2}$ components, separated in energy by 0.84 eV at an intensity of 2 : 1. The main phosphorus species in these HTBPs is phosphate centred at 134.5 eV.[25] In HTBP150, the appearance of a new speciation at 137.8 eV indicated that a novel stable P bond was formed thanks to the higher HT

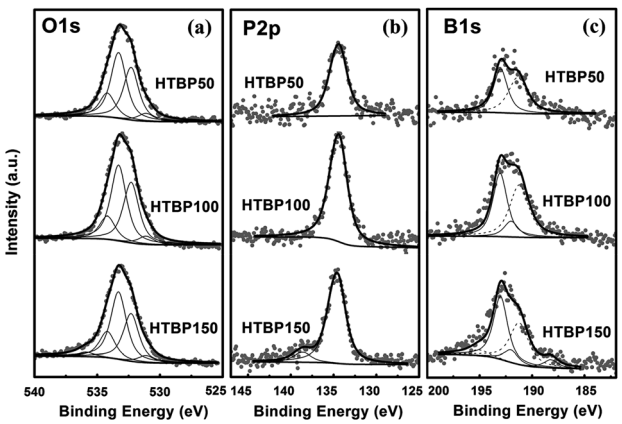

Fig. 4 XPS spectra of (a) O_{1s}, (b) P_{2p}, (c) B_{1s} for HTBP50, HTBP100 and HTBP150. The dark grey slash curves were noted as P_{2s} species overlapped in the B_{1s} spectra. The empirical atomic sensitivity factors of P_{2s} to P_{2p} were set to 0.65 according to previous study.[23]

temperature. Meanwhile, the fitting of B_{1s} XPS spectra are more complex since B_{1s} were overlapped by P_{2s}. Therefore, a subtraction of P_{2s} curves was required before further distinguishing the B species. In the calibrated B_{1s} spectra, the curves were split into

Table 1 N_2 adsorption and ICP analysis of HTBP samples

Sample	S_{BET}/m^2 g^{-1}	S_{meso}/m^2 g^{-1}	V_p/cm^3 g^{-1}	V_{meso}/cm^3 g^{-1}	D_p/nm	a_0/nm	Content/wt%	
							B	P
HTBP50	659	384	0.67	0.53	6.2	12.3	0.77	2.15
HTBP100	610	371	0.59	0.47	6.3	11.7	0.95	3.09
HTBP150	590	376	0.60	0.49	6.3	12.2	1.20	3.30

three groups centred at around 188.2, 192.0, and 193.0 eV, assigning to B–C, B–P, and B–O bonds, respectively.[7,26] The B–P bond appeared only when the HT temperature is higher than 100 °C. The details of these functional groups were listed in Table 2. It can be seen that increasing the HT temperature was accompanied by the obvious increases of C–O, C═O, and oxidized species. However, the multiplication almost ceased when the HT temperature is above 100 °C. Instead, the concentrations of these species were stabilized at a certain level, but a new B group with a B–P bond is generated at 100 °C and a new P speciation was formed when the HT temperature reached 150 °C. Bearing a binding energy close to that of halides, this new P speciation was supposed to originate from the interaction between the phosphorus source and HCl, due to the harsh synthesis conditions. However, the actual species is still not fully determined.

According to the above results, the HT temperature played a significant role in improving heteroatom introduction in the hydrothermal doping process. This was supposed to be attributed to the reaction of boric acid and phosphoric acid (Fig. 5) during the self-assembly. Under strong acidic conditions, both cross-linked phenols and F127 will be protonated, and interact with anions *via* coulombic forces according to the $S^+X^-O^+$ mechanism.[8] Meanwhile, B can react with P to form boron phosphate under hydrothermal conditions,[27] and hence drastically increase the solubility of B in the reaction system. The dehydration process was enhanced when employing a higher HT temperature and thus more complex containing B and P will be obtained and incorporated into the polymer matrix. When the concentration of boron phosphate anions is high enough, some of them may be further integrated and form crystals at the interface of aqueous solution and organic sol, while others were trapped in the organic matrix in amorphous forms. This is confirmed by the wide-angle XRD patterns of HTBP100 carbonized at 600 °C (Fig. 5).

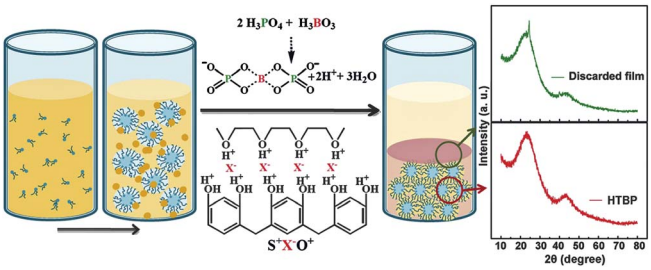

Fig. 5 The scheme of the hydrothermal doping process. The lower XRD pattern is of HTBP100 carbonized at 600 °C. The upper XRD pattern is the discarded interface film, which formed during the HT treatment, further carbonized at 600 °C.

2.3 Thermal stability of B/P co-modified OMCs

TG-MS was also conducted to explore the thermal stability of these functional groups on the OMCs (Fig. 6). According to TG-profiles, a higher HT temperature leads to less weight loss during hydrolysis in Ar atmosphere, from 15.7% (HTBP150) to 19.1% (HTBP100) to 23.4% (HTBP50). Correlated with MS spectra, the extra weight loss of low-temperature samples (HTBP50) was mainly attributed to desorption of H_2O above 750 °C and of CO at temperatures between 400 and 800 °C. The desorption of H_2O was confirmed to be originated from the condensation of adjacent phenolic or carboxylic acid groups,[28] while phenols, ethers, and carbonyls can produce CO peaks at temperature between 400 and 700 °C.[29] Many unreacted dissociative phenol-derived groups were tracked in the carbon matrix when the HT temperature was not high enough. In other words, it seems that a higher HT temperature activated resorcinol polymerization and resulted in a better cured precursor. Moreover, along with higher temperature, the enhancement of CO_2 desorption between 400 and 600 °C compensated that of at high temperature (800 to 900 °C) in HTBP50, indicating that some lactone species were transformed into carboxylic acid groups or their ancestors in HTBP100 and HTBP150, consistent with the XPS results. More interestingly, obvious desorption peaks of H_2O, CO, and CO_2 are observed simultaneously at the temperature of 250 °C in the case of HT150. Since all the HTBPs were hydrolyzed at 600 °C, thus, the dramatic desorption of 250 °C in HTBP150 was assumed to originate from species adsorbed on the carbon

Table 2 XPS results of HTBP samples

		Content/wt%		
Element	B.E./eV	HTBP50	HTBP100	HTBP150
O	531.1 (Quinone)	0.4	0.4	0.5
	532.3 (C═O)	2.8	3.3	3.1
	533.3 (C–O)	3.5	4.2	4.4
	534.2 (C–OH)	1.3	1.3	1.7
	535.9 (H_2O adsorb.)	—	—	0.3
	Total content	8.1	9.2	10.0
B	188.2 (B–C)	0	0	0.1
	192.0 (B–P)	0	0.3	0.3
	193.0 (B–O)	0.8	1.1	1.2
	Total content	0.8	1.4	1.6
P	134.5 (P–O)	2.3	3.4	3.2
	137.8 (P–X)	0	0	0.4
	Total content	2.3	3.4	3.6

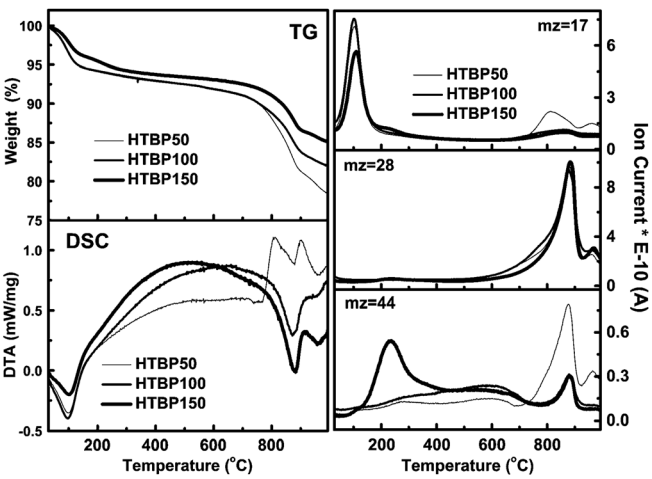

Fig. 6 (a) TG, (b) DSC, and (c) MS profiles of HTBP50, HTBP100 and HTBP150 in Ar at a heating rate of 10 °C min^{-1}.

surface in a manner similar to that on a metallic surface, consistent with O_{1s} XPS. However, such a phenomenon only happened on HTBP150, indicating that the new generated B- and/or P-containing speciation in HTBP150 is responsible for the strong adsorbability. In addition, no B- and P-containing species were detected during the whole pyrolysis process, indicating that B and P were firmly embedded in the carbon matrix. Besides, DSC patterns revealed smart endothermic peaks at around 840 and 960 °C in HTBPs corresponding to the desorption of CO and CO_2, respectively, which is consistent with the TG and MS results. Another peak at around 800 °C in HTBP50 can be attributed to the release of H_2O originating from the condensation of phenolic groups.

2.4 B/P co-modified OMCs as a supercapacitor electrode MC

The obtained HTBPs were evaluated as the electrodes of supercapacitors in a three-electrode cell. The testing of electrochemical performance was carried out on in a 6.0 M KOH electrolyte at a scan rate of 2.0 mV s^{-1} and a potential window from −1.0 V to 0.0 V. The results were listed in Table 3. Compared with previous reports, the specific capacitances of HTBPs were higher than those of B-OMC (0.19 F m^{-2}), P-OMC (0.24 F m^{-2}), BP-OMC (0.25 F m^{-2}) and heteroatom-free OMC (0.16 F m^{-2}) synthesised at room temperature and ambient pressure.[8] Meanwhile, the surface area is another significant factor for the final practical capacitance. Fortunately, thanks to the abundance of meso- and ultra-fine mesopores, the surface area of these HTBPs was *ca.* 600 m^2 g^{-1}, therefore, the gravimetric specific capacitance can be as high as *ca.* 180 F g^{-1}. Fig. 7 shows the specific capacitance cyclic voltammetry (CV) curves of (a) HTBP50, HTBP100, and HTBP150 at a scan rate of 5.0 mV s^{-1} and (b) HTBP100 at scan rates between 2.0 and 100 mV s^{-1}. At the scan rate of 5.0 mV s^{-1}, the forward and reverse capacitance were enlarged with the HT temperature and presented almost the same shape of symmetric and square CV curves. However, a slight bulge at around 0.7 eV was observed on HTBP150 in the discharge curve, indicating that B/O/P-containing species afford pseudo-capacitance. In another aspect, the gradually distorted shape of the CV curves as a function of scan rate in Fig. 7b indicated that a longer response time was required for fast charging and discharging. The ion-diffusion in the electrode is at a relatively slow rate. Such a phenomenon described an eating angle of a typical rectangular EDLC curve, in which one of the angles is drastically smoothed and seems to be eaten out and disappears, when the discharging started. This was assumed to be attributed to the poor conductivity of the HTBPs with a low carbonization temperature (600 °C).

Subsequently, electrochemical impedance spectroscopy (EIS) was employed to analyze the resistance and interpret the electrochemical kinetic behaviour on HTBPs. Fig. 7c shows the

Table 3 Specific capacitance and resistance of HTBP samples

Samples	Capacitance/F m^{-2}	Capacitance/F g^{-1}	R_i/Ω	R_{ct}/Ω
HTBP50	0.24	158	0.24	0.86
HTBP100	0.29	174	0.27	0.59
HTBP150	0.30	177	0.38	0.74

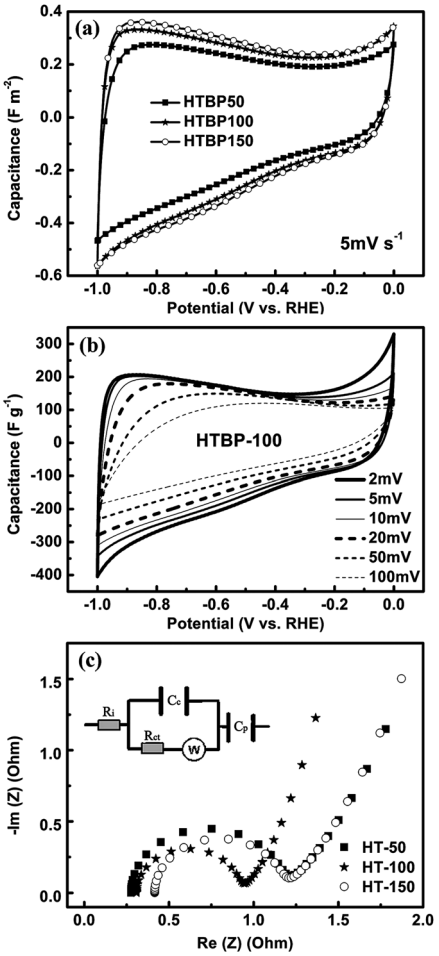

Fig. 7 (a) CV curves of HTBP50, HTBP100, and HTBP150 measured at 5 mV s^{-1}, (b) CV curves of HTBP100 measured at 2, 5, 10, 20, 50, and 100 mV s^{-1} in 6.0 M KOH, and (c) Nyquist plot of impedance spectra for HTBP50, HTBP100, and HTBP150.

Nyquist plots of BP-OMCs with different hydrothermal temperatures, using an equivalent circuit to simulate the capacitive and resistive element (show inset).[30] This circuit comprises the internal resistance (R_i), the contact resistance (R_{ct}) and capacitance (C_c), the Warburg diffusion attributed to the ion migration through the electrode (Z_w) and the capacitance inside the pores (C_p). According to the fitting parameters listed in Table 3, the internal resistances of all samples were below 0.4 Ω, indicating a promising conductivity of the test system. Meanwhile, the contact resistance (R_{ct}) with aqueous solution reached an optimized value of 0.59 Ω when applying a HT temperature of 100 °C. The R_{ct} which emerged at high frequency is reflected by the semicircle and demonstrates the charge transfer resistance at the interface between the electrolyte and electrode. The dramatic variation of R_{ct} was assumed due to the enhanced introduction of B and P species to the surface. According to the XPS results, B and P species were introduced mainly *via* hydrophilic oxygen bridges and subsequently increased the polarity of the carbon surface and facilitated the contact between it and the aqueous electrolyte. This can be explained by the fact that the R_{ct} of our B/P-modified carbons are much lower than that of 1∼2.5 Ω

reported in ordinary mesoporous carbon.[31] Particularly when employing a higher HT temperature, enhanced oxidized B and P species introduction further improved the charge transfer at the interface. However, in spite of a large amount of B and P being introduced, the R_{ct} of HTBP150 increased to 0.74 Ω and can be explained by new speciation generation. According to TG-MS and XPS results, these new generated species intend to adsorb a large amount of CO_2 and H_2O, and thus block the contact between the electrode surface and the electrolyte.

In this contribution, the dominated improvement of capacitor performance was carried out when increasing the HT temperature from 50 to 100 °C. According to the XPS results, though more oxygen was introduced along with B and P, they were mainly in the forms of C═O and C–O. However, quinone is the oxygen-containing speciation that was confirmed to contribute a lot to the pseudo-capacitance, thus, it can be postulated that functional groups containing P–O, B–O, as well as B–P bonds were the positive functions of capacitance. Meanwhile, other P-containing groups (like B.E. = 137.8 eV) and –OH groups introduced along with them showed no significant benefit, *per contra* inhibited the ionic diffusion and increased the resistance. Therefore, the positive function of B and P species was attributed to: on one hand, their oxygen-containing groups which were expected to increase the acidity of the carbon surface, and hence adsorb more ions when applying a high voltage; and on the other hand, the improvement of surface polarity, due to the introduction of n- and/or p-type heteroatoms, may increase the number of charge carriers and result in a higher capacitance. Both of these variations can lead to a higher capacitance and superior capacitor performance. However, which is the dominant factor is still under investigation.

3. Conclusions

B and P dual-modified OMCs were obtained by a facile hydrothermal strategy. The content and the speciation of heteroatom introduction were dependent on the hydrothermal temperature. Generally, B and P elements were introduced in the form of oxygen-containing groups and may interact mutually as the hydrothermal temperature is increased. Moreover, the heteroatom modification *via* such a hydrothermal strategy showed a stable and highly homogeneous distribution of B and P on the surface. The as-obtained HTBPs were applied as the supercapacitor electrodes. They showed superior capacitor performance when compared with our previously reported B/P co-modified OMCs synthesised at room temperature and ambient pressure.[8] The dramatic improvements of capacitance can be attributed to the introduction of oxidized B and P species.

4. Experimental

4.1 Chemicals

Pluronic F127 ($EO_{106}PO_{70}EO_{106}$) was supplied by Sigma-Aldrich and has an average molecular weight of 12 600. Resorcinol, formaldehyde (37 wt%), HCl (32 wt%), boric acid, and phosphoric acid (85 wt%) were all supplied by chemical plants in Germany. All the reagents were used as received without further purification. Deionized water was used in all experiments.

4.2 Synthesis procedure of B/P-modified mesoporous carbons

The boron- and phosphorus-modified mesoporous carbons were prepared *via* a hydrothermal strategy, using resorcinol as the carbon source, boric acid, and phosphoric acid as the heteroatom source to mediate the carbon properties. F127 was employed as the structure-directing agent in the multicomponent self-assembly process. For a typical synthesis recipe, 2.2 g (0.02 mol) resorcinol, 0.62 g (0.01 mol) boric acid, and 1.15 g (0.01 mol) phosphoric acid were dissolved in a solution containing 10.0 g water, 10.0 g ethanol, and 2.0 g F127 under magnetic stirring until the solution became transparent. Then, 0.6 g HCl (32 wt%) and 2.0 g formaldehyde (37 wt%) were added to the solution and stirred for another 1.5 h. The transparent homogeneous mixture was then transferred to an autoclave and heated to 50, 100, and 150 °C at a rate of 2.0 °C min^{-1} and reacted for 10 h. The solution separated into to layers, the upper solution was discarded and the interface film peeled off. Afterwards, the rest of the polymerized sticky monolith was dried overnight at 80 °C, and then heated under an Ar atmosphere at 600 °C for 2.0 h with a ramping rate of 2.0 °C min^{-1}. The final product is denoted as HTBP50, HTBP100, and HTBP150, respectively, depending on the hydrothermal temperature.

4.3 Characterization

Nitrogen sorption measurements were performed at −196 °C on a Micromeritics 2375 apparatus to determine the BET surface area and pore size distribution. The specific surface areas were calculated using the BET equation, the average mesopore diameters were estimated with adsorption branches based on the BJH model, and the micropore sizes were estimated based on Horvath–Kawazoe equation. To investigate the mesoporous ordering, low angle X-ray diffraction (XRD) patterns were collected using a PW3040/60 X' Pert PRO (PANalytical) diffractometer equipped with a Cu-Kα radiation source (λ = 0.15432 nm), operating at 30 kV, 40 mA. TG-MS analysis was conducted using a thermal gravimetric analysis (TGA) system comprising a TGA STA-449 Netsch apparatus equipped with a mass spectrometer (Pferffer Omnistar, Avi applied vacuum GmbH) as a detector under an Ar atmosphere. To reveal the surface properties, X-ray photoelectron spectroscopy (XPS) was conducted on an ESCALAB250 (Thermo VG Corporation) using Al Kα radiation (1486.6 eV, 15 kV, 10 mA, 150 W). Prior to fitting, a Shirley background was subtracted. All binding energies (B.E.) were corrected by charging of the sample by calibration on the graphitic carbon C_{1s} peak at a B.E. of 285 eV as a reference. The recorded spectra were fitted by a least square procedure to a product of Gaussian–Lorentzian functions. The concentration of each element was calculated from the area of the corresponding peak calibrated with the atomic sensitivity factor using C as a reference. Transmission electron microscopy (TEM) images were obtained on a Philips CM200 LaB_6 microscope operating at 200 kV, and electron energy loss spectroscopy (EELS) spectra and energy-filtered images were obtained on an FEI Cs-corrected Titan 80-300 microscope operating at 80.0 kV. The sample was ultrasonically dispersed in ethanol, and then a drop of the solution was deposited on a holey C/Cu TEM grid to be used for TEM and EELS characterization.

4.4 Electrochemical measurements

The electrochemical properties of the HTBPs were measured in an aqueous system (electrolyte: 6.0 M KOH) by a three-electrode arrangement. To prepare a working electrode, a mixture of an active material, carbon black, and poly(tetrafluoroethylene) (PTFE) with a weight ratio of 90 : 5 : 5 was ground together to form a homogeneous slurry. The slurry was squeezed into a film and then punched into pellets with a surface area of 1.0 cm^2 for each piece. The punched pellets with nickel foam on each side were pressed under 3.0 MPa and dried overnight at a temperature of 110 °C. Prior to the electrochemical tests, the electrodes were impregnated with electrolyte under vacuum for 2.0 h. The cyclic voltammetry (CV) tests and electrochemical impedance spectroscopy (EIS) profiles were performed using a VSP Bio-Logic potential workstation in a three-electrode cell in which a platinum slice was used as the counter electrode, and an Ag/AgCl reference electrode. Cyclic voltammograms were obtained within the potential window from −1.0 to 0 V at scan rates of 2, 5, 10, 20, 50, and 100 mV s^{-1}, respectively. The Nyquist plot was the original data without any fitting.

Acknowledgements

The authors greatly appreciate financial support by the EnerChem project of the Max Planck Society. The authors gratefully acknowledge Adriana Bernal Osorio, Gisela Lorenz, and Edith Kitzelmann for experimental assistance and fruitful discussions.

Notes and references

1 J. Lee, J. Kim and T. Hyeon, *Adv. Mater.*, 2006, **18**, 2073; C. D. Liang, Z. J. Li and S. Dai, *Angew. Chem., Int. Ed.*, 2008, **47**, 3696; Y. F. Shi, Y. Wan and D. Y. Zhao, *Chem. Soc. Rev.*, 2011, **40**, 3854.
2 S. Latil and L. Henrard, *Phys. Rev. Lett.*, 2006, **97**, 036803.
3 D. S. Su, J. Zhang, B. Frank, A. Thomas, X. C. Wang, J. Paraknowitsch and R. Schlogl, *ChemSusChem*, 2010, **3**, 169.
4 J. M. Carlsson and M. Scheffler, *Phys. Rev. Lett.*, 2006, **96**, 046806.
5 R. L. Liu, D. Q. Wu, X. L. Feng and K. Mullen, *Angew. Chem., Int. Ed.*, 2010, **49**, 2565.
6 D. S. Yu, Q. Zhang and L. M. Dai, *J. Am. Chem. Soc.*, 2010, **132**, 15127; S. B. Yang, X. L. Feng, X. C. Wang and K. Mullen, *Angew. Chem., Int. Ed.*, 2011, **50**, 5339.
7 D. W. Wang, F. Li, Z. G. Chen, G. Q. Lu and H. M. Cheng, *Chem. Mater.*, 2008, **20**, 7195.
8 X. C. Zhao, A. Q. Wang, J. W. Yan, G. Q. Sun, L. X. Sun and T. Zhang, *Chem. Mater.*, 2010, **22**, 5463.
9 H. L. Guo and Q. M. Gao, *J. Power Sources*, 2009, **186**, 551; T. Kwon, H. Nishihara, H. Itoi, Q. H. Yang and T. Kyotani, *Langmuir*, 2009, **25**, 11961.
10 S. L. Ding, S. J. Zheng, M. J. Xie, L. M. Peng, X. F. Guo and W. P. Ding, *Microporous Mesoporous Mater.*, 2011, **142**, 609.
11 M. Seredych, D. Hulicova-Jurcakova, G. Q. Lu and T. J. Bandosz, *Carbon*, 2008, **46**, 1475; D. Hulicova-Jurcakova, M. Seredych, G. Q. Lu and T. J. Bandosz, *Adv. Funct. Mater.*, 2009, **19**, 438.
12 D. Hulicova-Jurcakova, M. Seredych, G. Q. Lu, N. Kodiweera, P. E. Stallworth, S. Greenbaum and T. J. Bandosz, *Carbon*, 2009, **47**, 1576.
13 Q. Li, R. R. Jiang, Y. Q. Dou, Z. X. Wu, T. Huang, D. Feng, J. P. Yang, A. S. Yu and D. Y. Zhao, *Carbon*, 2011, **49**, 1248.
14 E. Frackowiak, G. Lota, J. Machnikowski, C. Vix-Guterl and F. Beguin, *Electrochim. Acta*, 2006, **51**, 2209; G. Lota, K. Lota and E. Frackowiak, *Electrochem. Commun.*, 2007, **9**, 1828; C. O. Ania, V. Khomenko, E. Raymundo-Pinero, J. B. Parra and F. Beguin, *Adv. Funct. Mater.*, 2007, **17**, 1828; E. Raymundo-Pinero, M. Cadek and F. Beguin, *Adv. Funct. Mater.*, 2009, **19**, 1032; D. Hulicova-Jurcakova, M. Kodama, S. Shiraishi, H. Hatori, Z. H. Zhu and G. Q. Lu, *Adv. Funct. Mater.*, 2009, **19**, 1800; L. Zhao, L. Z. Fan, M. Q. Zhou, H. Guan, S. Y. Qiao, M. Antonietti and M. M. Titirici, *Adv. Mater.*, 2010, **22**, 5202.
15 H. L. Wang, Q. M. Gao and J. Hu, *Microporous Mesoporous Mater.*, 2010, **131**, 89; D. Hulicova-Jurcakova, A. M. Puziy, O. I. Poddubnaya, F. Suarez-Garcia, J. M. D. Tascon and G. Q. Lu, *J. Am. Chem. Soc.*, 2009, **131**, 5026.
16 A. Villa, J. P. Tessonnier, O. Majoulet, D. S. Su and R. Schlogl, *ChemSusChem*, 2010, **3**, 241; Q. Shu, Z. Nawaz, J. X. Gao, Y. H. Liao, Q. Zhang, D. Z. Wang and J. F. Wang, *Bioresour. Technol.*, 2010, **101**, 5374; M. Hara, *ChemSusChem*, 2009, **2**, 129.
17 J. Zhang, X. Liu, R. Blume, A. H. Zhang, R. Schlogl and D. S. Su, *Science*, 2008, **322**, 73; B. Frank, J. Zhang, R. Blume, R. Schlogl and D. S. Su, *Angew. Chem., Int. Ed.*, 2009, **48**, 6913; B. Frank, M. Morassutto, R. Schomacker, R. Schlogl and D. S. Su, *ChemCatChem*, 2010, **2**, 644; J. H. Bitter, *J. Mater. Chem.*, 2010, **20**, 7312.
18 X. Jin, V. V. Balasubramanian, S. T. Selvan, D. P. Sawant, M. A. Chari, G. Q. Lu and A. Vinu, *Angew. Chem., Int. Ed.*, 2009, **48**, 7884.
19 A. H. Lu, J. J. Nitz, M. Comotti, C. Weidenthaler, K. Schlichte, C. W. Lehmann, O. Terasaki and F. Schuth, *J. Am. Chem. Soc.*, 2010, **132**, 14152.
20 Y. J. Zhang, T. Mori, J. H. Ye and M. Antonietti, *J. Am. Chem. Soc.*, 2010, **132**, 6294.
21 E. Frackowiak and F. Beguin, *Carbon*, 2001, **39**, 937; L. L. Zhang and X. S. Zhao, *Chem. Soc. Rev.*, 2009, **38**, 2520; D. S. Su and R. Schlogl, *ChemSusChem*, 2010, **3**, 136; E. Raymundo-Pinero, M. Cadek, M. Wachtler and F. Beguin, *ChemSusChem*, 2011, **4**, 943.
22 N. Baccile, M. Antonietti and M. M. Titirici, *ChemSusChem*, 2010, **3**, 246; M. M. Titirici and M. Antonietti, *Chem. Soc. Rev.*, 2010, **39**, 103; W. C. Zhu, X. L. Wang, X. Zhang, H. Zhang and Q. Zhang, *Cryst. Growth Des.*, 2011, **11**, 2935.
23 C. D. Wagner, L. E. Davis, M. V. Zeller, J. A. Taylor, R. H. Raymond and L. H. Gale, *Surf. Interface Anal.*, 1981, **3**, 211; R. J. Ward and B. J. Wood, *Surf. Interface Anal.*, 1992, **18**, 679.
24 R. Arrigo, M. Havecker, S. Wrabetz, R. Blume, M. Lerch, J. McGregor, E. P. J. Parrott, J. A. Zeitler, L. F. Gladden, A. Knop-Gericke, R. Schlogl and D. S. Su, *J. Am. Chem. Soc.*, 2010, **132**, 9616.
25 M. J. Ariza, E. Rodriguez-Castellon, R. Rico, J. Benavente, M. Munoz and M. Oleinikova, *J. Colloid Interface Sci.*, 2000, **226**, 151; A. M. Puziy, O. I. Poddubnaya, R. P. Socha, J. Gurgul and M. Wisniewski, *Carbon*, 2008, **46**, 2113.
26 R. Trehan, Y. Lifshitz and J. W. Rabalais, *J. Vac. Sci. Technol., A*, 1990, **8**, 4026.
27 C. J. Warren, R. C. Haushalter, D. J. Rose and J. Zubieta, *Chem. Mater.*, 1997, **9**, 2694; A. Baykal and M. Kizilyalli, *Turk. J. Chem.*, 2001, **25**, 425.
28 G. delaPuente, J. J. Pis, J. A. Menendez and P. Grange, *J. Anal. Appl. Pyrolysis*, 1997, **43**, 125.
29 J. H. Zhou, Z. J. Sui, J. Zhu, P. Li, C. De, Y. C. Dai and W. K. Yuan, *Carbon*, 2007, **45**, 785; J. L. Figueiredo and M. F. R. Pereira, *Catal. Today*, 2010, **150**, 2.
30 G. H. Xu, C. Zheng, Q. Zhang, J. Q. Huang, M. Q. Zhao, J. Q. Nie, X. H. Wang and F. Wei, *Nano Res.*, 2011, **4**, 870; C. W. Huang, C. H. Hsu, P. L. Kuo, C. T. Hsieh and H. S. Teng, *Carbon*, 2011, **49**, 895.
31 W. Li, F. Zhang, Y. Q. Dou, Z. X. Wu, H. J. Liu, X. F. Qian, D. Gu, Y. Y. Xia, B. Tu and D. Y. Zhao, *Adv. Energy Mater.*, 2011, **1**, 382.